California Water Research

June 2026

Comments on the Draft Shasta River Model Development Report

1. Introduction

The coupled LSPC–MODFLOW model is the culmination of a substantial, multi-year effort. It includes a successful calibration of Big Springs Creek and a Very Good full period fit at the Shasta River near Yreka gage. These are genuine accomplishments, and the modeling team's own Limitations and Recommendations (report Section 8) reflect a careful, self-critical development process.

These comments focus on incorporating the effects of climate change on the Shasta River watershed. Each recommendation builds on a limitation or recommendation the modeling team identified. Our central observation is one the report's own adaptive-development cycle anticipates (Step 6: "unsatisfactory model performance can indicate the influence of unrepresented physical processes").

The LSPC-MODFLOW model implicitly assumes a stationary precipitation-runoff partitioning, but the basin temperature and precipitation trends show a nonstationary climate. The model is strongest in the conditions it was calibrated to and weakest in the dry, multi-year drought conditions that now matter most.

This is a well-documented limitation of hydrologic models that hold their parameters fixed (Avanzi et al., 2020). Our recommendations describe an incremental path to address it.

Summary of recommendations

- **R1.** Report drought period and non-drought skill separately, not only as a full period aggregate.
- **R2.** Move toward a drought-conditional evapotranspiration parameterization, using HSPF's own capabilities.
- **R3.** Calibrate the spring/baseflow pathway as a process target, not only the integrated mainstem.
- **R4.** Report the snow model's skill stratified by temperature regime.
- **R5.** Expand the observational dataset toward the antecedent-state and groundwater storage constraints the basin currently lacks.

2. Climate context: a rapidly warming basin

The Shasta River basin lies in Siskiyou County, bounded by the Klamath Mountains on the west and, on the east, the Southern Cascade range rising to Mt. Shasta at about 14,000 ft. Its summer flow is sustained largely by springs issuing from the Mt. Shasta volcanic aquifer. The decisions the model supports will be made under a demonstrably changing climate. Independent analysis of PRISM temperature data (1896–2024) over the model's Shasta River watershed delineation shows the following.

Basin mean water year temperature trends are shown in Figure 1. Anomalies are relative to the first 30 year period, WY 1896 to 1925. The LOESS algorithm fits a nonlinear trend through the data by running a weighted local regression at each point, weighting nearby observations more heavily than distant ones. At the recent end of the record, this gives the latest years the most influence over the endpoint reported in the figures.

We use the STARS algorithm to detect step changes in temperature. It detects shifts in the mean of the time series (For more details, see Appendix A).

The graph shows that mean temperature increased in the early 20th Century during the dust bowl years and then decreased at midcentury. It has been warming rapidly and continuously since a shift around 1986. The basin mean water year temperature now has a 40 year LOESS endpoint of +2.87 °F over the 1895-1925 mean.

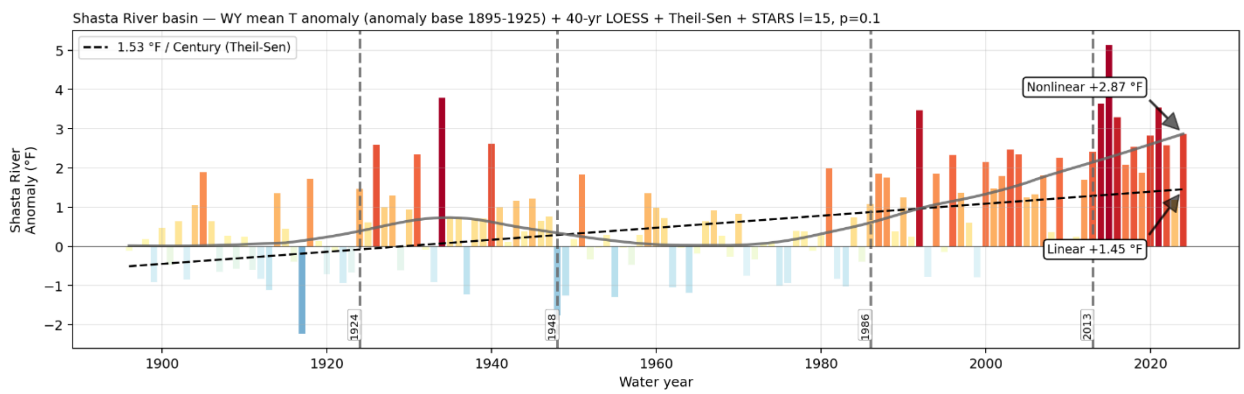

Figure 1. Basin mean water year temperature anomaly, 1896–2024 (PRISM, over the model watershed). Theil-Sen trend +1.53 °F/century (95% CI +0.99…+2.09; $p = 1.2 \times 10^{-6}$) with 40 year LOESS (endpoint +2.87 °F); regime shifts in WY 1986 and 2013.

The 1986 shift may have been part of with a global step increase in surface temperatures in the mid-1980s. Using CMIP5 simulations, Reid et al. (2015) attributed the step to the recovery from the 1982 El Chichón volcanic cooling, reinforced by anthropogenic warming. We also detect a step increase in temperature in water year 2013, the strongest whole basin annual mean shift in the record.

The 2013 step change coincides with a documented 2013/14 regime shift in eastern North Pacific annual mean sea surface temperature (Xiao and Ren 2023), which warmed the western North American coast. The basin's warming step therefore likely reflects a broader Pacific climate signal.

The 2013 step is also consistent with increases in effective radiative forcing in the annual *Indicators of Global Climate Change* assessments led by Piers Forster and a large international team of climate scientists. (Forster et al. 2023, 2024, 2025). These reports were developed to provide annual updates to key large-scale indicators assessed in the IPCC AR6 Working Group I report, using methods designed to remain traceable to AR6.

In the first IGCC update, published in 2023, Forster et al. showed that decadal trends in human-induced warming and anthropogenic effective radiative forcing had increased markedly since the IPCC 2021 AR6 assessment period, and that the inflection point was the early 2010s. The authors concluded that recent warming rates were unprecedented, with human activities causing recent global warming of more than 0.2°C per decade. Subsequent IGCC updates confirmed this result (Forster et al. 2023).

The 2013 STARS shift in temperature thus appears likely to be related to global increases in effective radiative forcing and Pacific Ocean temperature trends.

The step increase bears directly on how the model was tested. The basin's temperature regime steps upward at WY 2013, yet the coupled model's validation period (WY 1995–2012) is entirely in the cooler regime before that shift. The calibration period (WY 2013–2018) is after it, and the most recent and warmest years (WY 2019–2025) are beyond the model validation period altogether. The model is therefore validated on the pre-shift climate and never independently tested on the current, warmer regime. This matters most for the temperature-sensitive parts of the water balance, snow and evapotranspiration. See the snowpack discussion (Section 3).

Seasonal warming trends

Seasonal trends show that recent warming is uneven in three ways that matter for the basin's hydrology: it is largest in summer, it is concentrated at night, and it is spatially broad across the watershed. It also raises atmospheric evaporative demand year-round, and disproportionately in the dry season.

Seasonal warming trends are shown in Figure 2. By season, LOESS estimates a +1.75 °F nonlinear increase in fall (October–December), +1.65 °F in late winter (January–March), +2.66 °F in spring (April–June), and +5.41 °F in summer (July–September). The Theil-Sen summer warming rate is more than four times the fall rate. Summer is also the season of lowest flow and warmest water, so it is the season in which rising air temperature bears most directly on stream conditions.

The 1987 OND step increase and 1985 AMJ step increase occur within the post-El Chichon eruption global regime shift. The step increase in JFM in 1978 is concurrent with the 1977 Pacific Climate Shift. The step increase in AMJ in 2013 is concurrent with the 2013 step increase in eastern North Pacific SSTs.

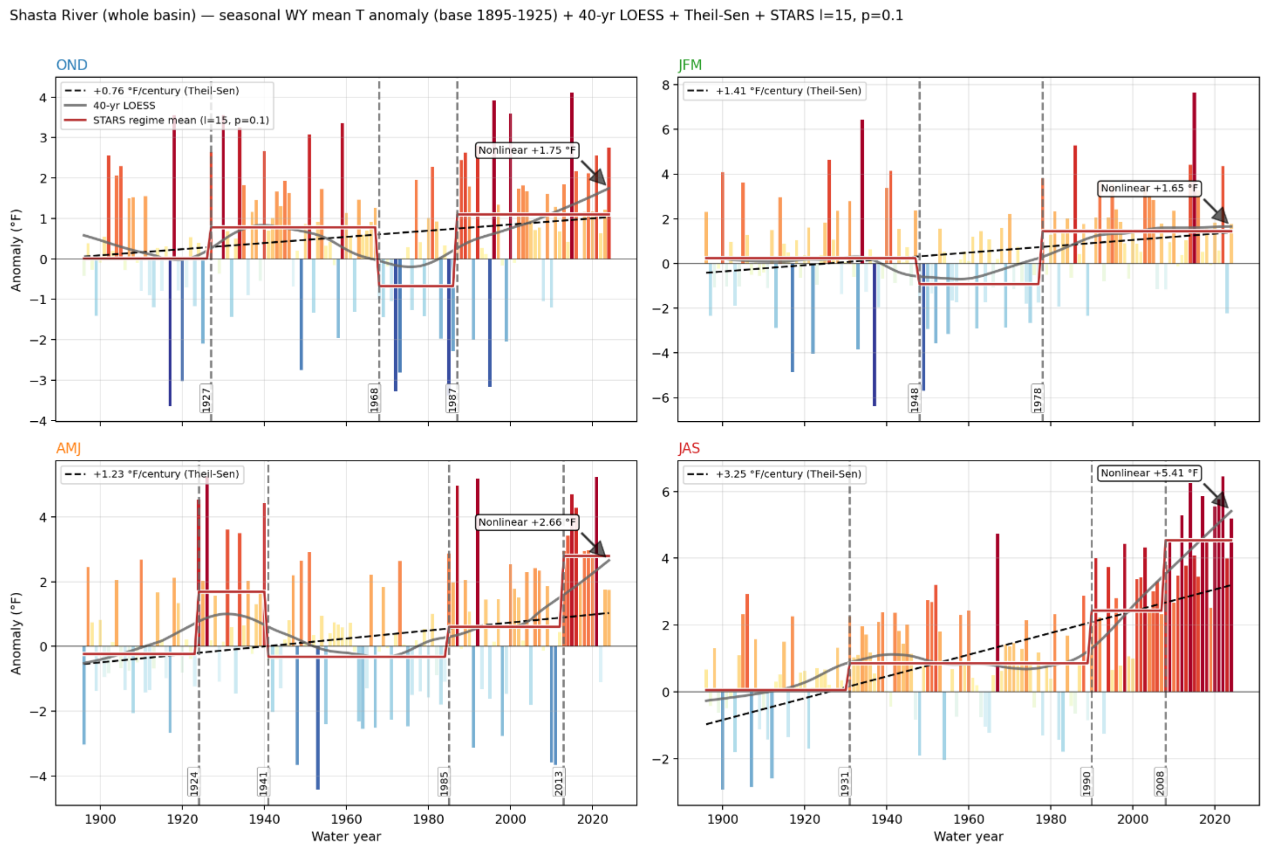

Figure 2. Basin temperature anomaly by water year quarter, 1896–2024 (PRISM), with Theil-Sen trend, 40 year LOESS, and STARS regime shifts. The summer quarter (July–September) warms fastest, at +3.25 °F/century, against +0.76 (fall), +1.41 (winter), and +1.23 (spring).

Minimum(Tmin) and Maximum(TMax) temperature trends are shown in Figure 3. Tmin and Tmax both show a step increase in 2013 and 2012, respectively. The warming is asymmetric between day and night. The linear trend shows overnight low temperatures rising about twice as fast as daytime highs, +2.14 versus +1.05 °F/century, and the nonlinear LOESS trend shows an increase of +3.57 versus +2.17 °F so the diurnal temperature range has narrowed significantly.

Streams shed heat at night, and warmer nights leave less of that natural cooling. A narrower diurnal range therefore makes it harder to keep water cold, especially through the summer, a direct concern for salmon.

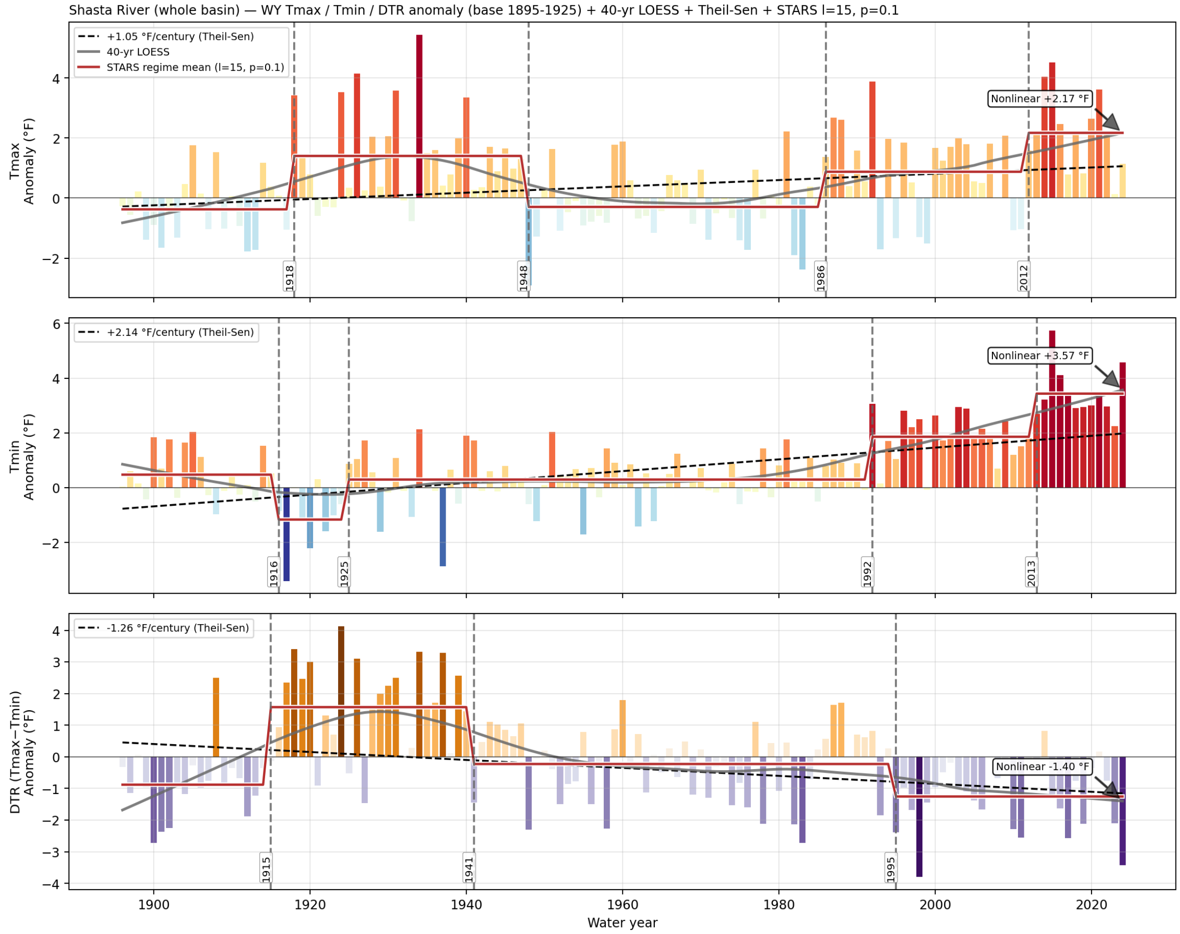

Figure 3. Basin daily maximum, daily minimum, and diurnal range (maximum minus minimum) temperature anomalies, 1896–2024 (PRISM), with Theil-Sen, 40 year LOESS, and STARS. Minimum temperature rises +2.14 °F/century, about twice the maximum at +1.05, so the diurnal range narrows by −1.26 °F/century.

Spatial warming trends

Figure 4 shows temperature shifts mapped to the model's subwatersheds. The trends in mean, maximum, and minimum temperature and in the diurnal range vary modestly across the basin. The enhanced warming that does appear is along the eastern margin, at the higher elevations where the higher Southern Cascade range rises. Minimum temperature warms faster than maximum in every subwatershed, so the diurnal range is narrowing across the whole basin.

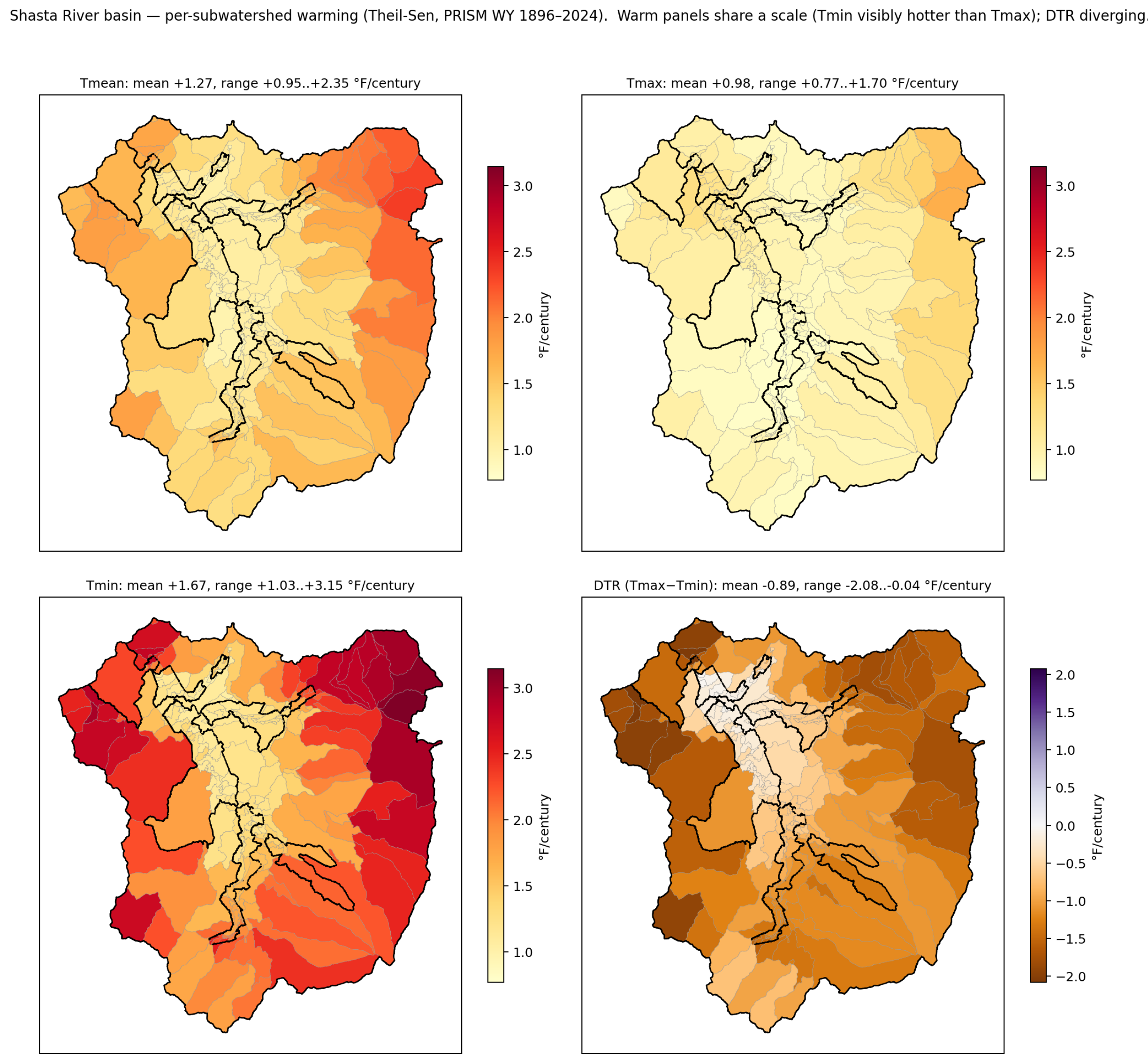

Figure 4. Warming trend by subwatershed (Theil-Sen, PRISM 1896–2024), mapped to the model's subwatersheds, for mean, maximum, and minimum temperature and for the diurnal range. The pattern is broadly uniform across the basin, with a slight enhancement along the higher eastern margin (the Southern Cascade range, rising to Mt. Shasta). Minimum temperature warms faster than maximum in every subwatershed, so the diurnal range narrows across the basin.

3. Snowpack loses skill in warm years

The higher altitude warming bears directly on snowpack. The snow calibration is excellent in cold and normal years but degrades sharply in the warmest ones. The report's Table 6-4 reports per-water year snow skill alongside the BRM snow season temperature. In cold and normal years, the fit is very good (Nash–Sutcliffe efficiency, NSE, of 0.86–0.97). But in the two warmest years it collapses. WY 2014 (snow-site mean 37 °F) has an NSE of just 0.04, essentially no skill, and WY 2015 (the warmest, 39 °F) an NSE of 0.43, with large volume biases (the model underpredicts snow water equivalent by 75% and 45% in those two years). The 2015–2016 El Niño shows the discrepancy from the other direction: in WY 2016 the model overpredicts peak snowpack by about 30% (over-shooting the observed peak by roughly 10 inches of snow water equivalent). Across all 16 snow calibration years (report Table 6-4, with the fuller per-year statistics in Table E-1, Appendix E), calibration skill is significantly anti-correlated with temperature (NSE vs snow season mean temperature, Pearson r = −0.62, p = 0.01; Spearman −0.70): the warmest years average an NSE of 0.23 versus 0.89 for the coolest. We independently confirm the poorly calibrated years were anomalously warm. The basin's cool season (Nov–Mar) PRISM temperature anomaly was +2.7 °C in WY 2015 (the warmest in the record) and positive in WY 2014.

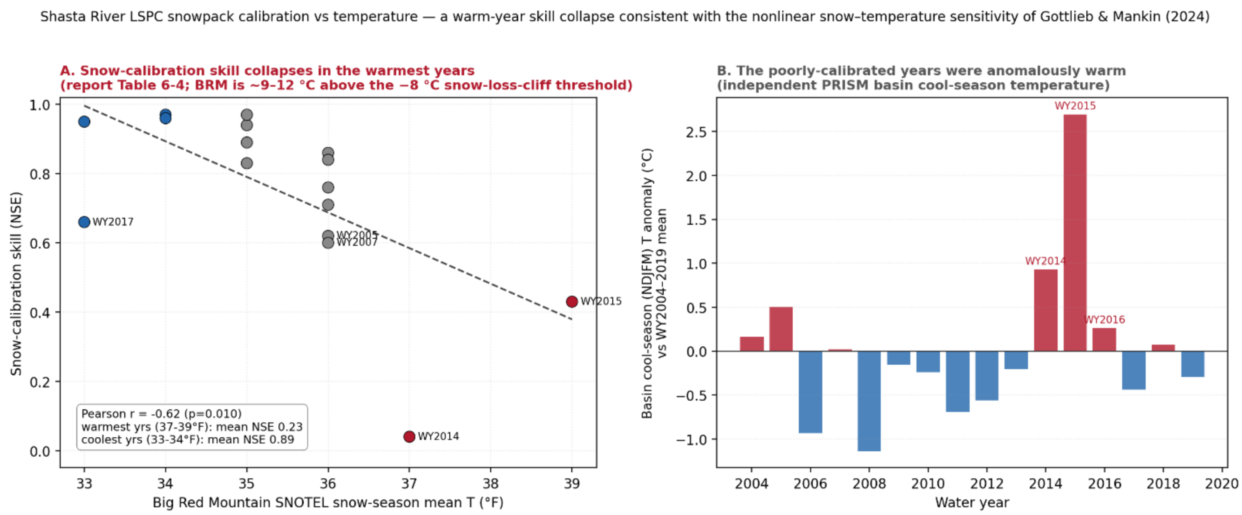

Figure 5. Shasta River LSPC snowpack calibration vs temperature. (A) Per-water year snow calibration skill (NSE; report Table 6-4) declines with the Big Red Mountain snow season mean temperature (Pearson r = −0.62, p = 0.01); the two warmest years (WY 2014, WY 2015) collapse to NSE 0.04 and 0.43. The site sits 9–12 °C above the −8 °C "snow-loss cliff" of Gottlieb & Mankin (2024). (B) The poorly calibrated years were anomalously warm, confirmed independently by the basin cool season (Nov–Mar) PRISM temperature anomaly (WY 2015 +2.7 °C).

This is consistent with the nonlinear snow–temperature sensitivity recently found by researchers. Gottlieb and Mankin (2024), a detection and attribution study spanning 169 Northern Hemisphere river basins (1981–2020), document a "snow-loss cliff". Snowpack becomes sharply more sensitive to each additional degree of warming once climatological winter temperature exceeds roughly −8 °C, and they attribute the Southwestern United States' declines, among the steepest in the hemisphere, to human influence. The BRM snow site sits at a snow season mean temperature of +0.6 to +3.9 °C, deep in the high-sensitivity regime where each degree of warming has an outsized effect on snowpack. A marginal, warm snow site of this kind is exactly where a snow model calibrated to a stationary temperature response will mispredict.

The model also appears to have a systematic timing bias related to snowpack. The report's composite (average-year) comparison of modeled versus observed snowpack at BRM (Appendix E) shows the model builds snow earlier: modeled snow water equivalent runs above observed through fall and winter, reaches a peak about 8.8% lower than observed, and melts out earlier, while the observed snowpack peaks later and persists further into spring and early summer. The total volume difference is small (+3.8%), so the error is not primarily one of amount but of phase. A snowpack that accumulates and melts too early shifts the modeled spring melt, runoff, and recharge earlier in the year.

The model's monthly streamflow calibration at Yreka (Fig 6-23, over the WY 2013–2018 calibration period) carries the same phase error in runoff: the model overpredicts early winter flow (modeled monthly medians sit above the observed interquartile range in November–January) and underpredicts the March–May spring-melt flow (modeled March is below the observed median, and May runs low). That is the streamflow signature of snow arriving as early winter runoff rather than as spring melt.

A plausible cause, consistent with the model's structure of fixed parameters, is that the snow parameters are calibrated as a single constant set across a period (WY 2013–2018) that spans both the extreme warm-drought years (WY 2014–2016) and more normal years. A fixed parameter set cannot reproduce both a warm, early melting regime and a cooler, later-melting one. The calibration could settle on a compromise that, pulled toward the warm years, accumulates and melts snow too early on average, matching neither regime well. The warm-year skill collapse and the early runoff bias could thus be two faces of the same limitation: a stationary snow calibration asked to represent a basin that now moves between regimes.

The model's validation currently does not test the warmer regime. The coupled model is calibrated on WY 2013–2018, the recent, hot period that includes the 2014–2016 warm drought, and validated on WY 1995–2012 (Fig 6-27). The most recent and warmest years, WY 2019–2025, fall outside the model calibration or validation period entirely. An independent validation on the post-2018 warm years would directly probe how well the model fits in the new climate regime.

Recommendation R4. Report the snow model's skill stratified by temperature regime (warm vs normal/cold water years), as recommended for streamflow in R1, so the warm-year skill is visible to decision makers rather than absorbed into a multi-year average. And, consistent with R2, consider whether the snow parameters can be made responsive to temperature (or the warm-year skill otherwise constrained) so the model tracks the nonlinear snow–temperature sensitivity rather than a single stationary one. Expanded snow observations within the basin or at higher elevation would directly support this and pair with the monitoring recommendation (R5).

4. Good aggregate streamflow calibration masks a weakness specific to drought

The model's full period skill at Yreka is genuinely good. The full record PBIAS is Very Good (~0; Table 6-14). But that aggregate conceals a clear, decision-relevant pattern when the record is decomposed:

- **By period.** The model fits its drought calibration period (WY 2013–2018) worse than its wetter validation period (WY 1995–2012): all-season PBIAS −12.7% vs −2.4%, dry season −22.7% vs −4.7%, and the highest 10% of flows −26.2% vs −12.3% (Tables 6-10, 6-12). A model that fits its drought period worse than its validation period is exhibiting the opposite of the usual pattern.
- **By flow condition.** Even over the full record, the model overpredicts storm and sub-median flows while underrepresenting baseflow: too much fast runoff, too little spring-fed baseflow, netting to a near-zero aggregate.
- **By location.** Two tributary gages, Little Shasta River and Shasta River near Edgewood, are rated Poor (Table 6-14; Edgewood ~60% bias). These are small, low-volume tributaries where PBIAS is inherently sensitive, so the binary Poor rating is the load-bearing point: good mainstem skill is not basin-wide skill.

The report concedes the substance of this directly: “the calibrated model tended to overestimate flows in the Dry Season” (p.125), and “simulating dry season and low flow conditions remain challenging.” We recommend that the model’s skill be reported by hydrologic regime so this pattern is visible to decision makers (R1).

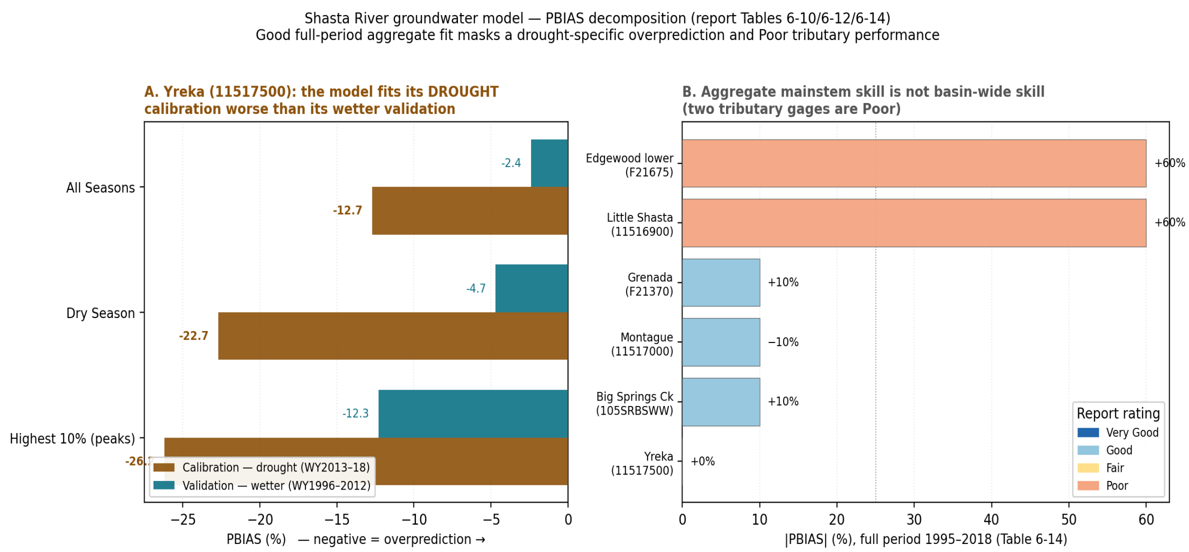

Figure 6. Decomposition of the model’s reported PBIAS (Tables 6-10/6-12/6-14). Left: the Yreka gage fits its drought calibration period far worse (−12.7% all-season, −22.7% dry, −26.2% peaks) than its wetter validation period (−2.4% / −4.7% / −12.3%). Right: full period |PBIAS| by gage, with mainstem and Big Springs Good/Very Good, but two tributary gages (Little Shasta, Edgewood) Poor. A good full period aggregate masks a drought-specific weakness.

5. The underlying issue: a stationary model for a nonstationary climate

One of the effects of increased temperature is an increase in evaporative demand and a resulting decrease in soil moisture for a given reduction in precipitation. This can be seen in decreasing regional Palmer Drought Severity Index (PDSI) trends.

Our analysis (Figure 7) found impaired runoff efficiency (Shasta River near Yreka WY outflow divided by basin precipitation) closely tracks the prior year's PDSI. There is a (lag-1 correlation r = +0.52 vs concurrent +0.32), a storage-memory signature of one year. Prior year PDSI has a stronger correlation than temperature with impaired runoff efficiency (Figure 8).

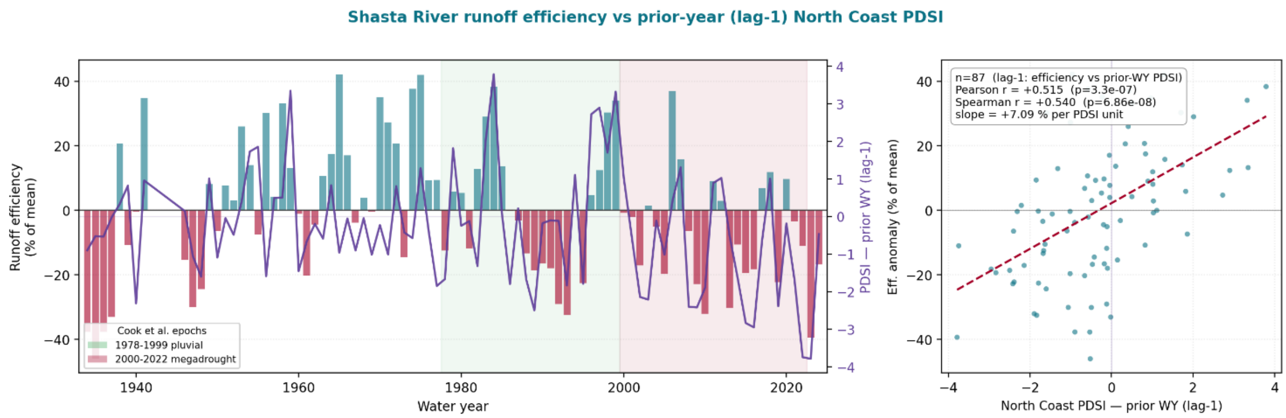

Figure 7. Shasta River near Yreka (USGS 11517500) runoff-efficiency anomaly versus the prior water year's North Coast (Division 1) PDSI. Efficiency tracks prior-year moisture (lag-1 Pearson r = +0.52) more strongly than the concurrent year (r = +0.32), a signature of groundwater storage memory and a concrete behavior the model should be expected to reproduce.

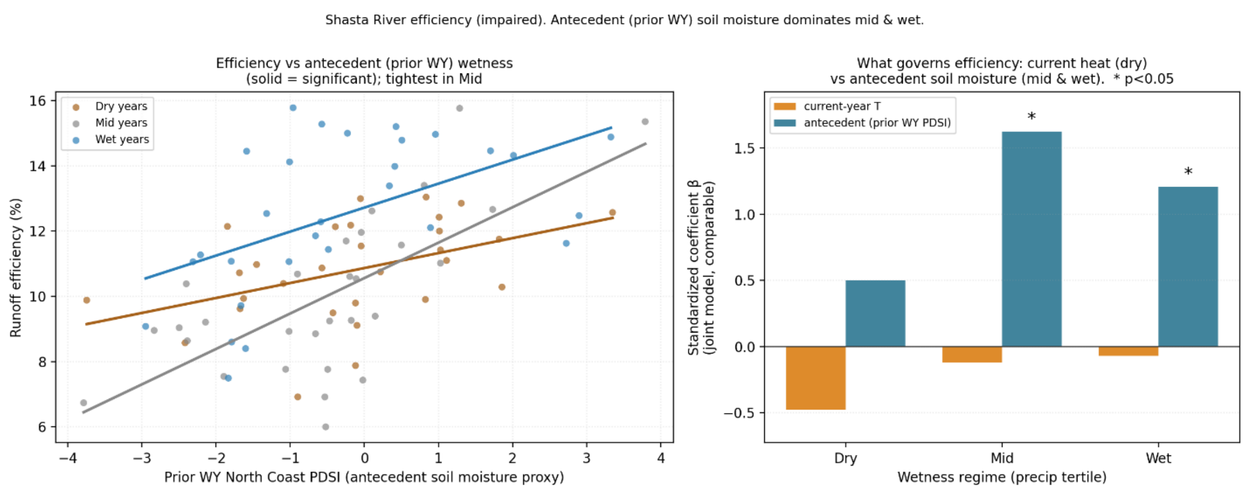

Figure 8 Shasta River near Yreka runoff efficiency: correlation with current-year heat versus antecedent soil moisture, by precipitation terciles (Dry, Mid, Wet). (Left) Annual runoff efficiency versus prior WY North Coast (Division 1) PDSI. The positive relationship is tightest in the Mid precipitation tercile; solid fit lines are significant at $p < 0.05$. (Right) Standardized coefficients from a joint regression of efficiency on current-year basin temperature and prior water year PDSI, fit separately within each tercile. Antecedent soil moisture is the dominant control in the Mid ($\beta = +1.63$, $p < 0.001$) and Wet ($\beta = +1.21$, $p = 0.005$) regimes. Only in Dry years are the two comparable, and there both are marginal (temperature $\beta = -0.48$, $p = 0.10$; soil moisture $\beta = +0.50$, $p = 0.08$).

Avanzi et al. (2020) corroborate the shift in runoff efficiency. Studying the Feather River watershed, they found multi-year droughts shifted the precipitation–runoff relationship (−18% to −39% depending on subsurface character) and concluded the mechanisms "remain largely unknown and are not well represented in hydrologic models."

A model with fixed parameters cannot reproduce a persistent, drought-triggered shift of partitioning of precipitation toward evapotranspiration and away from runoff. The Shasta model's calibration may show this fingerprint directly. The model fits the drought period worse than its wetter validation period, exactly the pattern expected when a stationary partitioning struggles to track a drought-shifted one.

Specifically, LSPC's land segment hydrology is the HSPF (Stanford Watershed Model) PWATER algorithm, operated here with time-invariant calibrated parameters. The parameters that govern how precipitation is partitioned among runoff, evapotranspiration, infiltration, and groundwater are single constants held fixed across the entire 1991–2023 simulation. They include infiltration (INFILT), the soil moisture storages (UZSN, LZSN), and the lower zone ET term (LZETP). The model therefore represents a stationary rule for partitioning precipitation into runoff.

Section 8 (R2) recommends an incremental, HSPF-native path toward a climate-elastic ET partitioning.

6. The model underrepresents the spring network that sustains baseflow

The lower Shasta River has a spring-dominated hydrograph. Big Springs Creek alone averages ~50–100 cfs and supplies roughly 95% of irrigation-season baseflow. The report calibrates Big Springs Creek separately and well (Figures 6-30/6-31), a genuine success that these comments credit.

The other springs, however, are not reproduced. We emphasize that these springs were not calibration targets. By the report's account, their flow estimates "were not used for calibration purposes but were used to assess the model performance… to identify… the model areas that are deficient in reproducing stream flows." Table 6-8 is thus the modeling team's own diagnostic self-assessment. By that self-assessment, the model reproduces only about 18% of the assessed spring discharge, and just 1.4% of the discrete springs represented as MODFLOW drain (DRN) boundaries (86.8 cfs observed vs 1.2 cfs simulated). Several substantial springs are simulated at essentially zero, including Alcove (47 → 0 cfs) and Cold (13 → 0 cfs). These springs are passive DRN sinks fixed at land-surface elevation, and they are the part of the spring/groundwater sources that sustain summer low flows, so their underrepresentation matters most for the model's stated application (R3).

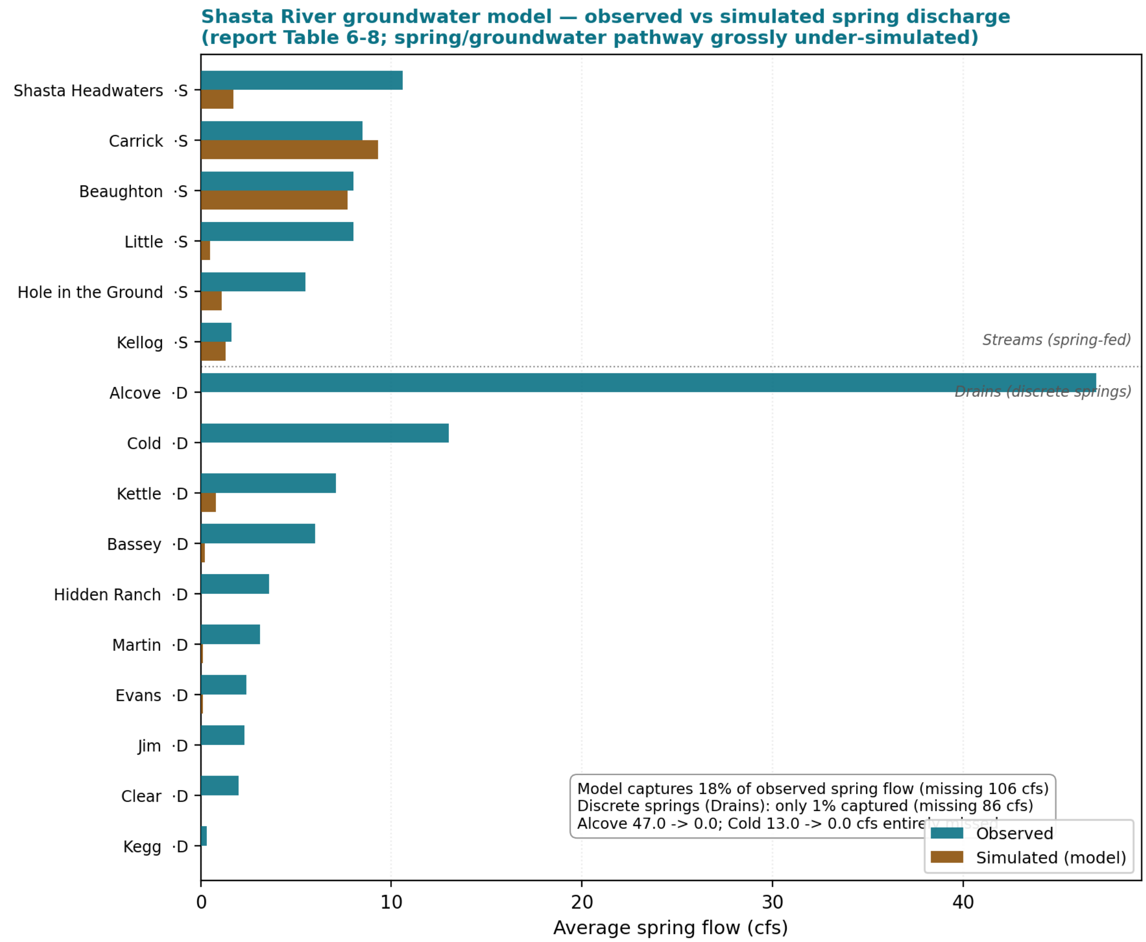

Figure 9. Observed vs simulated average spring discharge for the springs in the model report's Table 6-8 (drains and spring-fed streams). The model reproduces ~18% of the assessed spring discharge and ~1.4% of the discrete drain springs; the largest, Alcove (47 cfs observed), is simulated at zero.

We note this is a problem of spatial distribution, not a problem of volume. The model conserves mass and matches the integrated mainstem; the missing discrete spring discharge is compensated by other, calibrated fluxes. The concern is that the model reproduces the right total through the wrong spatial and process pathways, which limits its reliability for spatially explicit pumping-impact questions.

7. Climate context: precipitation shifts in recent decades

Precipitation has been declining in recent decades and the wet season has been contracting. Water year precipitation shows a declining tendency that is not statistically significant as a linear trend (Theil-Sen −41 mm/century, $p = 0.30$). The decadal signal is clearer. The 30 year LOESS endpoint is −126 mm, about −19% below the 1896–1977 baseline of ~670 mm/yr. The decline is concentrated in the core wet season (January–March, −25 mm/century), and regime shift analysis detects a step to drier conditions at water year 2007 (annual) and 2001 (Jan–Mar).

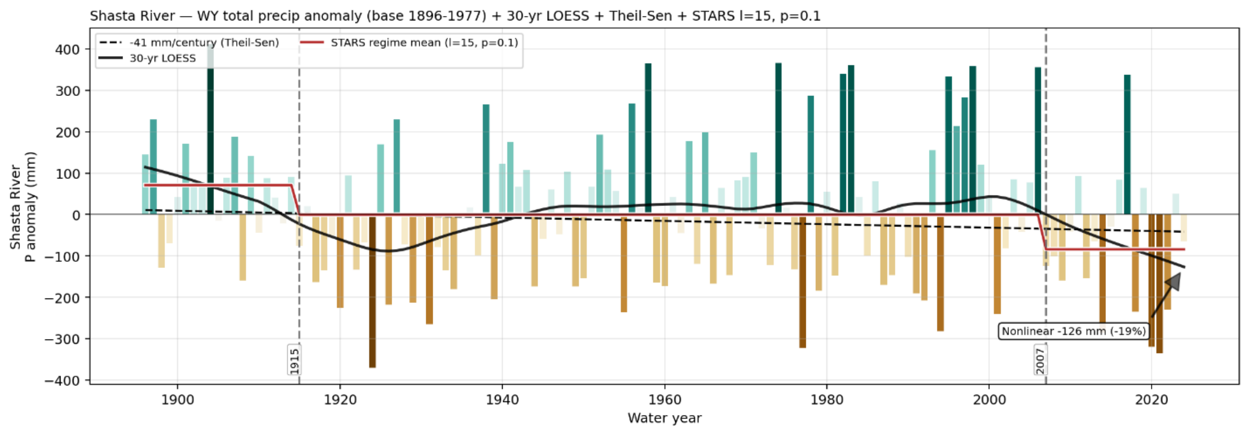

Figure 10. Basin water year total precipitation anomaly, 1896–2024 (PRISM). Theil-Sen −41 mm/century (not significant; p = 0.30) with 30 year LOESS (endpoint −126 mm, ≈ −19% below the ~670 mm/yr baseline); STARS dry shift at WY 2007.

The precipitation shifts will directly affect recharge, and the report documents such a shift. Using the Basin Characterization Model (Flint et al. 2021) over the contributing area draining to Big Springs, the report's Figure 6-32 shows annual average recharge varying across the century and stepping to lower values in the recent decades: by 25-year averaging period, about 115 cfs in 1896–1925, 102 in 1926–1950, 118 in 1951–1975, 107 in 1976–2000, and 99 in 2001–2024. The most recent period sits roughly 15 to 20 cfs below the early-century and mid-century values, and the report reads the record as century-scale variability with a shift toward lower recharge.

The decline seems likely related to the contracting wet season and JFM precipitation declines, as explained below, as well as the temperature and snowmelt drivers documented in sections 2 and 3. Unfortunately, recharge calibrated to the 2001–2024 regime may be a snapshot of a still-declining quantity.

Seasonal shifts

A seasonal decomposition shows the structure of the annual trend. Shoulder season precipitation (October–December and April–June) rose through the late twentieth century and then fell steeply in the twenty-first (Figure 11). That late-century rise is broadly consistent with the 1978–1999 Southwestern North America (SWNA) megapluvial of Cook et al. (2025), the wettest interval in their 1,200-year reconstruction, and the subsequent decline with the SWNA megadrought that Williams et al. (2022) found had become the driest 22-year span (2000–2021) in at least twelve centuries. The basin lies in the northwestern portion of the SWNA domain (30–45°N, 105–125°W) used in that work.

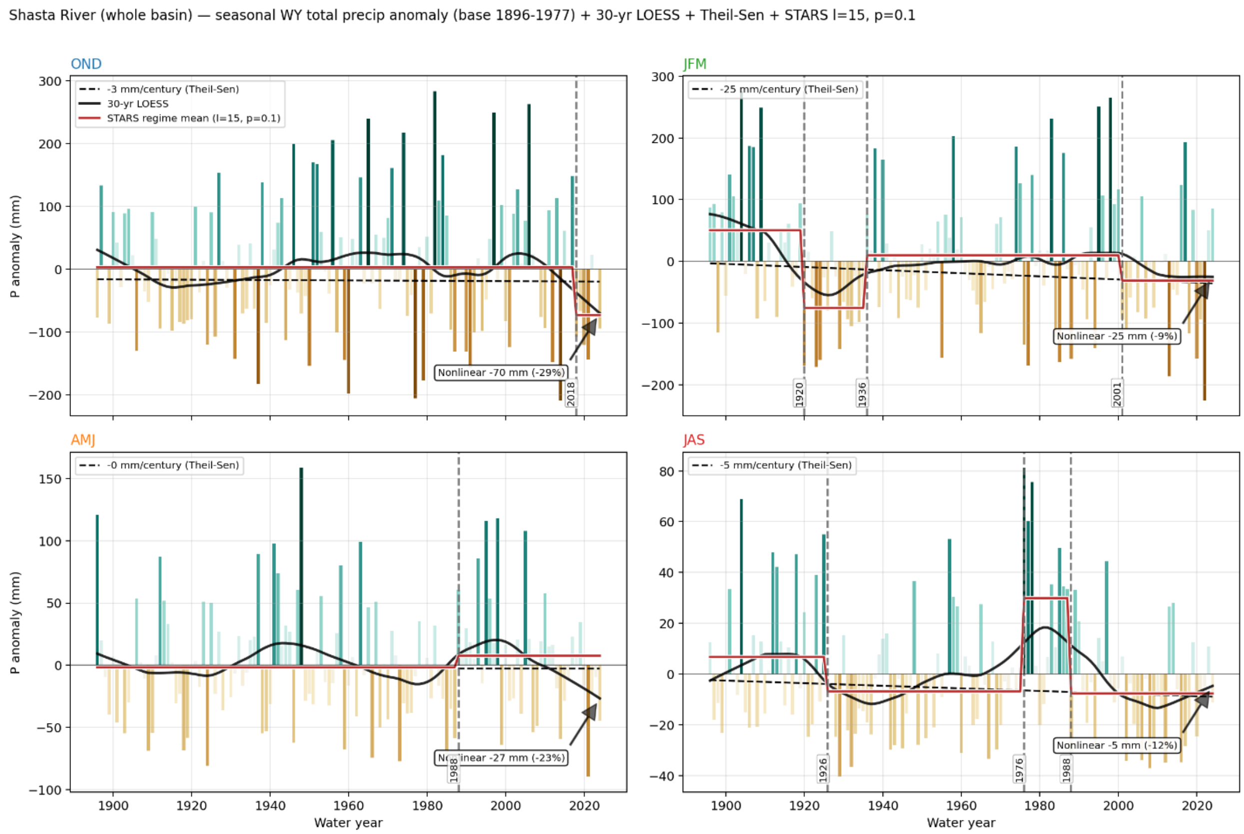

Figure 11. Basin seasonal water-year total precipitation anomaly by quarter (OND, JFM, AMJ, JAS), 1896–2024 (PRISM, base 1896–1977), with Theil-Sen, 30-year LOESS, and STARS (l=15, p=0.10). The core wet season (JFM) carries the steepest decline (−25 mm/century) and a STARS dry shift at WY 2001; the shoulder seasons (OND, AMJ) rise through the late twentieth century and fall in the twenty-first.

Atmospheric river and Pacific Ocean trends

The month groups used for our seasonal analysis (OND, JFM, AMJ, JAS) are shifted by a month from calendar seasons so that JFM spans the peak landfalling Pineapple Express atmospheric river season. The Pineapple Express cluster (Hawaii-genesis, 180–210°E) corresponds to the central North Pacific to western United States route of Pan et al. (2024), and to the Pineapple Express type of Zhang and Villarini (2018).

Pan et al. found that ARs using this route landfall predominantly in late winter and that AR genesis hotspots shift eastward from the western to the central North Pacific from early spring to late winter. Both Pan et al. (2024) and Zhang and Villarini (2018, r = +0.13) report that Pineapple Express landfalls correlate with a positive Pacific Decadal Oscillation sea surface temperature pattern.

Two climate indices are used to characterize the state of the Pacific Ocean that generates California's atmospheric rivers. The Pacific Decadal Oscillation (PDO) is the leading pattern of North Pacific sea surface temperatures, and it tends to hold a warm or cool phase for decades. The Multivariate ENSO Index (MEI) measures the El Niño and La Niña state of the tropical Pacific. Both indices stepped to a warm regime in 1977 and to a cooler regime in 1999. Klavans, DiNezio, Clement, et al. (2025) found that approximately 53 percent of observed PDO variability since around 1950 is forced rather than internal. Current forcing suggests that the cooler PDO is likely to continue for the near term.

This is the large-scale Pacific setting in which the basin's precipitation has declined (Figure 11; details in Appendix A).

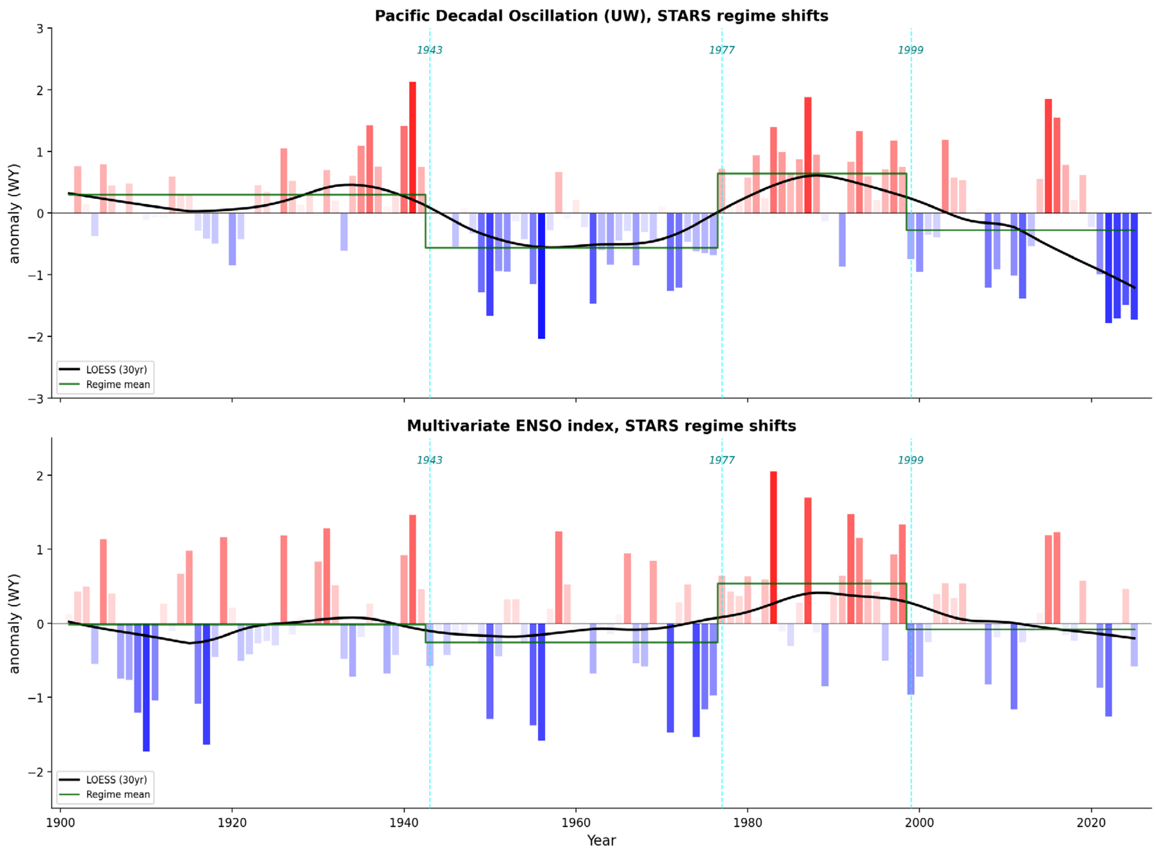

Figure 12. Pacific climate state by water year, 1901–2025. Anomalies of the Pacific Decadal Oscillation (PDO, top; UW/Mantua) and the Multivariate ENSO Index (MEI, bottom; stitched MEIv2 and historical extension), each relative to their 1901–2025 average. Red is warm or El Niño-leaning, blue is cool or La Niña-leaning. Black curve, 30-year LOESS; green line, STARS regime mean; dashed lines, regime-shift years (STARS l=15, p=0.10). The two indices shift together at 1943, 1977, and 1999, marking a cool North Pacific regime (1943–1976), the warm, El Niño-prone regime of 1977–1998, and the cool regime since 1999.

This wet season decline is consistent with an independently documented reduction in landfalling Pineapple Express atmospheric rivers (ARs). These ARs originate over the subtropical Pacific near Hawaii and track northeast toward the West Coast. Pan et al. (2025) report that landfalling Pineapple Express ARs have declined significantly in the Pacific Northwest. Pan et al.'s western North America analysis box extends south to about the California–Oregon border (~42 °N), so the Shasta River basin (~41.7–41.9 °N) lies immediately south of, and adjacent to, that southern boundary. The authors attribute this anomaly largely to strengthened ridging between Hawaii and western North America.

Using the ARLiD catalogue, we analyzed California atmospheric rivers by genesis cluster. Our results were consistent with Pan et al.'s findings. Landfalling Pineapple Express ARs reaching Northern California (36–42°N) in January through March fall by roughly half, from about 1.1 to 0.6 per year, across the 1999/2000 shift (Figure 13).

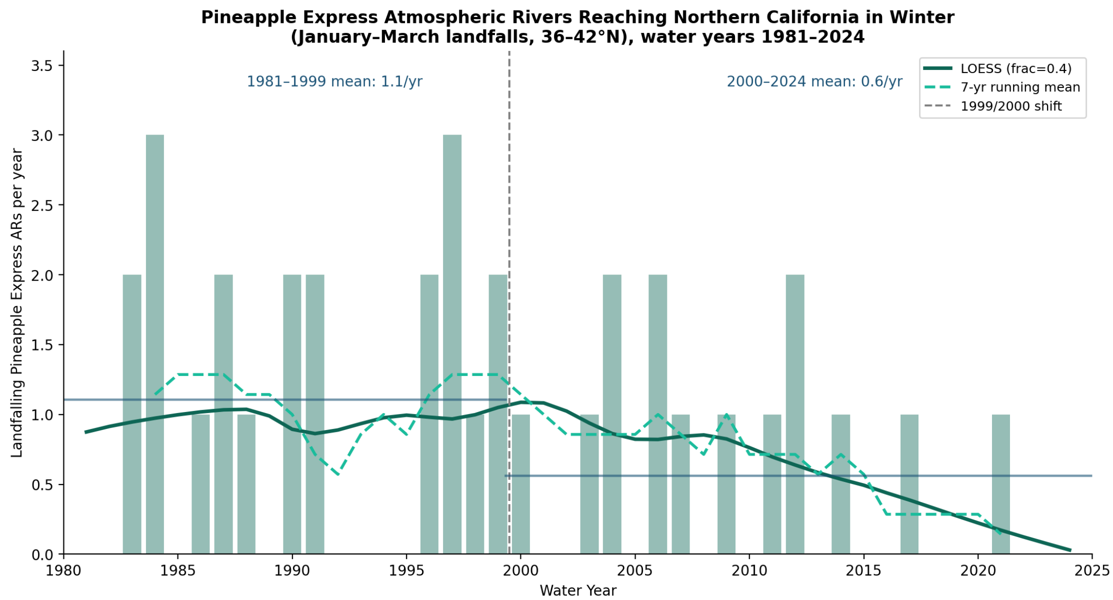

Figure 13. Pineapple Express atmospheric rivers landfalling in Northern California (36–42°N) in winter (January–March), by water year, 1981–2024 (ARLiD). Annual counts (bars) with a 7-year running mean and LOESS; the dashed line marks the 1999/2000 megapluvial-to-megadrought boundary. The winter Northern California landfall rate falls by roughly half, from about 1.1 per year in 1981–1999 to 0.6 per year in 2000–2024.

Splitting the record at the 1999/2000 SWNA megapluvial-to-megadrought boundary, Pineapple Express landfalls decline from the earlier to the later period, with the reduction concentrated in the January and March peak of the cool season (Figure 14).

The Pineapple Express suppression over the adjacent Pacific Northwest, and the regionally observed post-1999 decline in Pineapple Express landfalls thus offers a potential mechanism for the basin's wet season precipitation decline.

That decline coincides with the cool PDO epoch since 1999 (Figure 11), which is likely partly forced (Klavans et al. 2025). But the sharpest recent decline likely reflects the emergent North Pacific ridging and marine heatwaves of the 2010s more than the PDO shift. Persistent West Coast ridging, including the 2012–2016 "Ridiculously Resilient Ridge," diverts atmospheric rivers away from California (Gibson et al. 2020), and the recent North Pacific warming pool marine heatwaves and resulting atmospheric ridging have been attributed to anthropogenic greenhouse forcing (Barkhordarian et al. 2022).

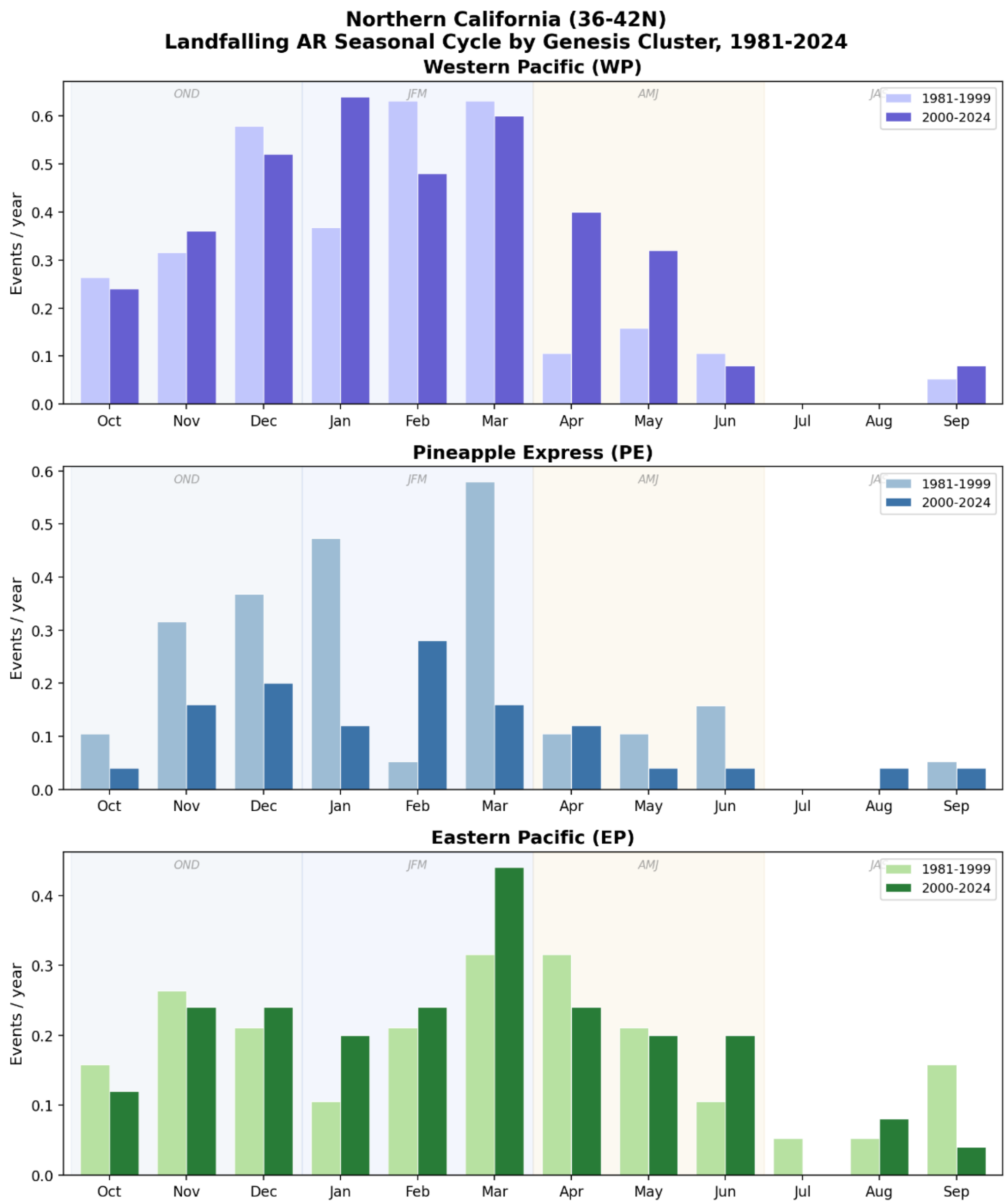

Figure 14. Northern California landfalling atmospheric river seasonal cycle by genesis cluster (Western Pacific, Pineapple Express, Eastern Pacific), comparing the 1981–1999 (megapluvial) and 2000–2024 (megadrought) periods (events/month). Pineapple Express declines in the megadrought period, concentrated in the January and March cool-season peak. Source: ARLiD California-landfalling AR catalog.

8. Recommendations

These recommendations are constructive and incremental. Each builds on a limitation or recommendation already in the report's Section 8.

R1. Report drought and non-drought skill separately. Add regime-stratified skill reporting at the Yreka gage, alongside the existing full period and calibration/validation splits. (PBIAS and flow-duration skill stratified by multi-year drought vs normal/wet years; NSE only as a secondary metric, as it is unstable on short low flow samples) This is pure post-processing of existing output, and it makes the drought-specific weakness visible to decision makers. A transparent drought-year definition (e.g., multi-year North Coast PDSI ≤ −1) suffices.

R2. Move toward a drought-conditional ET parameterization. To represent the multi-year hysteresis, the team may wish to consider whether HSPF's capabilities could be used: (a) activate the monthly-varying lower zone ET and interception tables (MON-LZETPARM, MON-INTERCEP), which the model currently does not use; and/or (b) use Special Actions to shift the lower zone storage/ET parameters to a drought set-point when an antecedent-moisture or PDSI index crosses a threshold. We support the report's recommendation to add climate-change scenario runs, and add that such scenarios are only meaningful if the underlying ET partitioning is itself climate-elastic; otherwise they inherit a stationary response. *Scope note:* monthly variation alone encodes a fixed within-year cycle, not a between-year drought shift. The Special-Actions option (b) is the more capable path but introduces parameters that require the expanded monitoring of R5.

R3. Calibrate the spring/baseflow pathway as a process target. Add the discrete spring discharges (Table 6-8 sites) and a baseflow-separation target at Yreka as explicit, multi-objective calibration objectives, so the split between surface runoff and percolation (governed by the HSPF INFILT parameter, which the report notes was "refined to reduce infiltration" in the southwestern area to better align predictions of shallow groundwater discharge with known springs and zones with a high water table, a change that, mechanically, also shifts water toward surface runoff) is constrained to reproduce the spring pathway rather than only the aggregate hydrograph. Prioritize the volumetrically dominant springs (Alcove ~47 cfs, Cold ~13 cfs). It is neither necessary nor data-supported to force every 1–2 cfs drain to match.

R4. Report the snow model's skill stratified by temperature regime Group the per-water year snow skill the report already computes (Table 6-4) by temperature regime, warm versus normal/cold water years, and report the two groups separately alongside the multi-year calibration average. This makes the warm-year skill collapse visible to decision makers rather than absorbed into a favorable average: the two warmest years fall to NSE 0.04 (WY 2014) and 0.43 (WY 2015) against 0.86–0.97 in cold and normal years, with snow water equivalent underpredicted by 75% and 45%, and skill is significantly anti-correlated with snow season temperature (Pearson $r = -0.62$, $p = 0.01$). As with R1 for streamflow, this is pure post-processing of existing output, with no re-run. Consistent with R2, consider whether the snow parameters can be made temperature-responsive, or the warm-year skill otherwise constrained, so the model tracks the nonlinear snow–temperature sensitivity rather than a single stationary one.

R5. Expand the observational dataset toward antecedent-state and storage constraints. We strongly support the report's recommendation to expand the calibration dataset, and add a targeting rationale: prioritize data that constrain multiyear storage memory and the antecedent-state dependence of runoff, namely paired groundwater-level time series at the discrete springs, and improved diversion/return flow accounting toward a synthetic near-natural baseflow series. The one-year storage memory lag we observe (Section 5) is a concrete validation test the model should be expected to pass once such data exist.

9. Conclusion

The coupled LSPC–MODFLOW Shasta River model is a substantial and well-documented body of work, with real successes in its Big Springs Creek and integrated-mainstem calibration. The recommendations above are intended to strengthen it for the specific decisions it will support (drought, summer low flow, groundwater pumping, and water rights) under a climate that is measurably warming and drying. The unifying theme is that a fixed parameter, stationary precipitation-runoff representation is least reliable in exactly the dry, multi-year drought conditions that now matter most, and that an incremental, HSPF-native path exists to address this, in step with the modeling team's stated limitations and recommendations.

Appendix A. Statistical methods for the climate figures

The temperature, precipitation, and Pacific-index figures in Section 2 and Section 7 are produced with the data and statistical methods described here.

Data and basin averaging. The series are derived from PRISM monthly grids (mean, minimum, and maximum temperature, and precipitation) aggregated over the model report's delineation of the basin and subwatersheds. Each monthly basin average is computed over the PRISM cells whose centers fall inside the basin polygon, weighting each cell by the cosine of its latitude. Monthly values are combined on a water year basis (October through September) into the water year and seasonal series shown. Temperature anomalies are referenced to a 1896–1925 WY base period, following the NCEI convention, and reported in degrees Fahrenheit. Precipitation anomalies are referenced to a 1896–1977 base period and reported in millimeters. Trends, smoothers, and regime shift tests are computed on these series.

LOESS smoothing. The LOESS algorithm fits a nonlinear trend through the data by running a weighted local regression at each point, weighting nearby observations more heavily than distant ones. Clarke and Richardson (2021) proposed continuous local regression on a 40 year window (plus or minus 20 years) as an alternative to the IPCC's linear trend methods for warming projections. They validated the method against observational datasets and two large global climate model ensembles, MPI-GE and CSIRO Mk3.6.0, and found it substantially less sensitive to internal variability than ordinary least squares (OLS), with lower long-term bias and lower short-term uncertainty. We use a 40 year window for temperature, following that work, and a shorter 30 year window for precipitation, to show decadal-scale variation.

Theil-Sen trend and Mann-Kendall significance. The Theil-Sen slope estimator is a nonparametric linear trend estimator. It computes the median of all pairwise slopes between data points. Unlike OLS regression, it does not assume normally distributed residuals and is robust to outliers, which makes it better suited to nonstationary climate series in which the variance changes over time and extreme events produce non-Gaussian deviations. Slopes are reported per century with a 95% confidence interval. Significance is assessed with the Mann-Kendall rank correlation test (Mann 1945; Kendall 1975), the nonparametric trend test conventionally paired with the Theil-Sen slope. The p-values in the figure captions are Mann-Kendall values.

STARS regime shift detection. The STARS algorithm (Sequential T-test Analysis of Regime Shifts; Rodionov 2004; Overland et al. 2008) detects statistically significant step changes in the mean of a time series. A step change is a discrete shift from one mean level to a higher or lower one, as distinct from a gradual linear trend. Applied to the basin mean climate anomalies, STARS identifies the years at which the series moved from one mean state to another. We run it on the raw per water year series with a cutoff length parameter of 15 years and a significance level of $p = 0.10$. The detected shift years appear as the dashed vertical guides in the figures.

Pacific climate indices (Figure 12). We use the University of Washington (Mantua) Pacific Decadal Oscillation and a Multivariate ENSO Index assembled from the modern MEIv2 (1979 onward) spliced to its historical extension, each averaged over the water year (October through September) and clipped to the common 1901–2025 period. Each index is plotted as a departure from its own 1901–2025 average, so red marks warm, El Niño-leaning years and blue marks cool, La Niña-leaning years. The black curve is a 30-year LOESS smoother showing the slow decadal variation. The dashed vertical lines mark regime shifts, the years when the index steps from one multi-year average level to another, detected with the STARS method described above (Rodionov 2004; Overland et al. 2008); the green line shows the average level within each regime. For these indices we show two of the method's standard settings: a stricter one (cutoff length 15 years, significance 0.10) that isolates the major decadal regimes, and a more sensitive one (cutoff length 10 years, significance 0.30) that also resolves shorter regimes.

Atmospheric river clusters (Figures 13 and 14). Landfalling California atmospheric rivers are taken from the ARLiD catalog (1980–2024) and classified by genesis longitude into three clusters: Western Pacific (genesis west of 180°E), Pineapple Express (180–210°E), and Eastern Pacific (east of 210°E) (Figure 15).

Western Pacific ARs ($n = 642$) are trans-Pacific systems with the longest median duration (206 h) and a median California landfall at 39.3°N. Pineapple Express ARs ($n = 263$) form over the central North Pacific near Hawaii, run about half as long (102 h), and land at a median 39.0°N. Eastern Pacific ARs ($n = 359$) are short-fetch systems generated off the West Coast, the briefest (67 h), and with peak landfall farther south (median 34.7°N).

This genesis-based grouping follows the typology of Zhang and Villarini (2018) and corresponds to the cross-Pacific routes of Pan et al. (2024), whose central North Pacific to United States route is the Pineapple Express cluster.

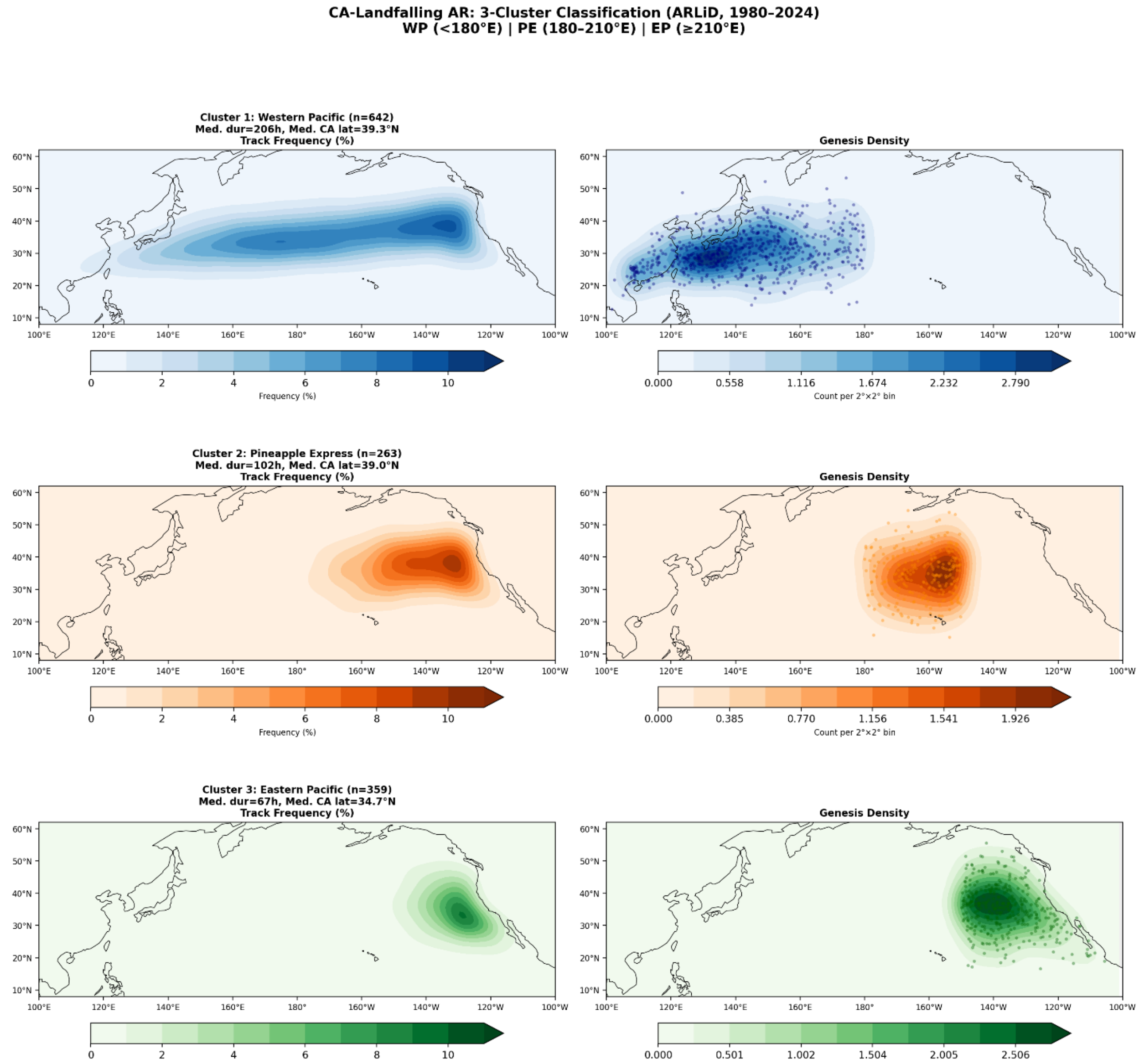

Figure 15. Three-cluster classification of California-landfalling atmospheric rivers by genesis longitude (ARLiD, 1980–2024). Each landfalling AR is assigned to one of three clusters by genesis longitude: Western Pacific (WP, west of 180°E), Pineapple Express (PE, 180–210°E), and Eastern Pacific (EP, east of 210°E). The left column maps each cluster's track frequency (the percent of that cluster's tracks crossing each grid cell) and the right column its genesis density (where those ARs form, counts per 2° by 2° bin).

References

Avanzi, F., Rungee, J., Maurer, T., Bales, R., Ma, Q., Glaser, S., and Conklin, M. (2020). Climate elasticity of evapotranspiration shifts the water balance of Mediterranean climates during multi-year droughts. *Hydrology and Earth System Sciences* **24**, 4317–4337. doi:10.5194/hess-24-4317-2020.

Barkhordarian, A., Nielsen, D. M., and Baehr, J. (2022). Recent marine heatwaves in the North Pacific warming pool can be attributed to rising atmospheric levels of greenhouse gases. *Communications Earth & Environment* **3**, 131. doi:10.1038/s43247-022-00461-2.

California State Water Resources Control Board (2026). *Shasta River Model Development* (Draft). [coupled LSPC–MODFLOW model report; cited herein by section, table, and page.]

Clarke, D. C., and Richardson, M. (2021). The benefits of continuous local regression for quantifying global warming. *Earth and Space Science* **8**, e2020EA001082. doi:10.1029/2020EA001082.

Cleveland, W. S. (1979). Robust locally weighted regression and smoothing scatterplots. *Journal of the American Statistical Association* **74**, 829–836. doi:10.1080/01621459.1979.10481038.

Cook, B. I., Williams, A. P., Smerdon, J. E., Marvel, K., and Seager, R. (2025). Megapluvials in Southwestern North America. *AGU Advances* **6**(2), e2024AV001508. doi:10.1029/2024AV001508.

Flint, L. E., Flint, A. L., and Stern, M. A. (2021). The basin characterization model: a regional water balance software package. *U.S. Geological Survey Techniques and Methods* 6-H1, 85 p. doi:10.3133/tm6H1.

Forster, P. M., Smith, C. J., Walsh, T., Lamb, W. F., Lamboll, R., Hauser, M., Ribes, A., Rosen, D., Gillett, N., Palmer, M. D., Rogelj, J., von Schuckmann, K., Seneviratne, S. I., Trewin, B., Zhang, X., Allen, M., Andrew, R., Birt, A., Borger, A., … Zhai, P. (2023). Indicators of Global Climate Change 2022: Annual update of large-scale indicators of the state of the climate system and human influence. *Earth System Science Data*, *15*, 2295–2327. https://doi.org/10.5194/essd-15-2295-2023

Forster, P. M., Smith, C., Walsh, T., Lamb, W. F., Lamboll, R., Hall, B., Hauser, M., Ribes, A., Rosen, D., Gillett, N. P., Palmer, M. D., Rogelj, J., von Schuckmann, K., Trewin, B., Allen, M., Andrew, R., Betts, R. A., Borger, A., Boyer, T., … Zhai, P. (2024). Indicators of Global Climate Change 2023: Annual update of key indicators of the state of the climate system and human influence. *Earth System Science Data*, *16*, 2625–2658. https://doi.org/10.5194/essd-16-2625-2024

Forster, P. M., Smith, C., Walsh, T., Lamb, W. F., Lamboll, R., Cassou, C., Hauser, M., Hausfather, Z., Lee, J.-Y., Palmer, M. D., von Schuckmann, K., Slangen, A. B. A., Szopa, S., Trewin, B., Yun, J., Gillett, N. P., Jenkins, S., Matthews, H. D., Raghavan, K., … Zhai, P. (2025). Indicators of Global Climate Change 2024: Annual update of key indicators of the state of the climate system and human influence. *Earth System Science Data*, *17*, 2641. https://doi.org/10.5194/essd-17-2641-2025

Gibson, P. B., Waliser, D. E., Guan, B., DeFlorio, M. J., Ralph, F. M., and Swain, D. L. (2020). Ridging associated with drought across the western and southwestern United States: characteristics, trends, and predictability sources. *Journal of Climate* **33**(7), 2485–2508. doi:10.1175/JCLI-D-19-0439.1.

Gottlieb, A. R., and Mankin, J. S. (2024). Evidence of human influence on Northern Hemisphere snow loss. *Nature* **625**, 293–300. doi:10.1038/s41586-023-06794-y.

Kendall, M. G. (1975). *Rank Correlation Methods* (4th ed.). London: Charles Griffin.

Klavans, J.M., DiNezio, P.N., Clement, A.C., et al., Human emissions drive recent trends in North Pacific climate variations. Nature 644, 684-692 (2025). DOI:10.1038/s41586-025-09368-2

Mann, H. B. (1945). Nonparametric tests against trend. *Econometrica* **13**, 245–259. doi:10.2307/1907187.

Overland, J., Rodionov, S., Minobe, S., and Bond, N. (2008). North Pacific regime shifts: definitions, issues and recent transitions. *Progress in Oceanography* **77**, 92–102. doi:10.1016/j.pocean.2008.03.016.

Pan, M., Lu, M., and Lall, U. (2024). Diversity of cross-Pacific atmospheric river main routes. *Communications Earth & Environment* **5**, 378. doi:10.1038/s43247-024-01552-y.

Pan, M., Hu, S., Zaitchik, B. F., and Pan, W. K. (2025). Contrasting historical trends of atmospheric rivers in the Northern Hemisphere. *npj Climate and Atmospheric Science* **8**(1), 307. doi:10.1038/s41612-025-01191-w.

Reid, P.C. , Hari, R.E. , Beaugrand, G. , Livingstone, D.M. , Marty, C. , Straile, D. , Barichivich, J. , Goberville, E. , Adrian, R. , Aono, Y. , Brown, R. , Foster, J. , Groisman, P. , Hélaouët, P. , Hsu, H-H , Kirby, R. , Knight, J. , Kraberg, A. , Li, J. , Lo, T-T , Myneni, R.B. , North, R.P. , Pounds, J.A. , Sparks, T. , Stubi, R. , Tian, Y. , Wiltshire, K.H. , Xiao, D. and Zhu, Z (2015) Global impacts of the 1980s regime shift. Global Change Biology. doi: 10.1111/gcb.13106.

Rodionov, S. N. (2004). A sequential algorithm for testing climate regime shifts. *Geophysical Research Letters* **31**, L09204. doi:10.1029/2004GL019448.

U.S. EPA. Loading Simulation Program in C++ (LSPC); HSPF and BASINS Technical Note 6 (hydrologic-process and parameter definitions for the PWATER land segment module). USEPA (2017a,b).

Williams, A. P., Cook, E. R., Smerdon, J. E., Cook, B. I., Abatzoglou, J. T., Bolles, K., Baek, S. H., Badger, A. M., and Livneh, B. (2020). Large contribution from anthropogenic warming to an emerging North American megadrought. *Science* **368**, 314–318. doi:10.1126/science.aaz9600.

Williams, A. P., Cook, B. I., and Smerdon, J. E. (2022). Rapid intensification of the emerging southwestern North American megadrought in 2020–2021. *Nature Climate Change* **12**, 232–234. doi:10.1038/s41558-022-01290-z.

Xiao, D., and Ren, H.-L. (2023). A regime shift in North Pacific annual mean sea surface temperature in 2013/14. *Frontiers in Earth Science* **10**, 987349. doi:10.3389/feart.2022.987349.

Zhang, W., and Villarini, G. (2018). Uncovering the role of the East Asian jet stream and heterogeneities in atmospheric rivers affecting the western United States. *Proceedings of the National Academy of Sciences* **115**(5), 891–896. doi:10.1073/pnas.1717883115.

Secondary references cited as they appear in the model report: Jeffres et al. (2008, 2009); Nichols et al. (2008, 2010); Niswonger et al. (2011); Siskiyou County GSA (2021); Ward & Eaves (2011).

Data sources:

PRISM Climate Group (precipitation, Tmean/Tmin/Tmax, 1895–2024)

USGS NWIS daily discharge (gages 11517500, 11517000)

OpenET (ensemble actual ET)

NOAA nClimDiv Palmer Drought Severity Index (California North Coast Drainage, Division 1)

FAO-56 Penman-Monteith reference evapotranspiration.